# Reconstruction of MRI Data Encoded by Multiple Nonbijective Curvilinear Magnetic Fields

Fa-Hsuan Lin,[1,2]* Thomas Witzel,[2] Gerrit Schultz,[3] Daniel Gallichan,[3] Wen-Jui Kuo,[4] Fu-Nien Wang,[5]* Juergen Hennig,[3] Maxim Zaitsev,[3] and John W. Belliveau[2]

**Parallel imaging technique using localized gradients (PatLoc) uses the combination of surface gradient coils generating nonbijective curvilinear magnetic fields for spatial encoding. PatLoc imaging using one pair of multipolar spatial encoding magnetic fields (SEMs) has two major caveats: (1) The direct inversion of the encoding matrix requires exact determination of multiple locations which are ambiguously encoded by the SEMs. (2) Reconstructed images have a prominent loss of spatial resolution at the center of field-of-view using a symmetric coil array for signal detection. This study shows that a PatLoc system actually has a higher degree of freedom in spatial encoding to mitigate the two challenges mentioned above. Specifically, a PatLoc system can generate not only multipolar but also linear SEMs, which can be used to reduce the loss of spatial resolution at the field-of-view center. Here, we present an efficient and generalized image reconstruction method for PatLoc imaging using multiple SEMs without explicitly identifying the locations where SEM encoding is not unique. Reconstructions using simulations and empirical experimental data are compared with those using conventional linear gradients to demonstrate that the general combination of SEMs can improve image reconstructions. Magn Reson Med 68:1145–1156, 2012. ©2012 Wiley Periodicals, Inc.**

**Key words: MRI; nonlinear gradients; surface gradients; PatLoc; parallel MRI; time-domain reconstruction**

MR radiofrequency (RF) coil arrays have been introduced to generate images with high signal-to-noise ratio (SNR) and a large field-of-view (FOV) (1). Parallel MRI was then proposed to use distinct yet spatially correlated data among different channels of an RF coil array to enhance the spatiotemporal resolution of MRI at the cost of SNR (2,3). Different from parallel MRI using highly parallel RF detection, parallel imaging technique using localized gradients (PatLoc) (4) uses the combination of surface gradient coils and an RF receiver array to improve the efficiency of MRI spatial encoding and to reduce the peripheral nerve stimulation hazard. PatLoc is a generalization of non-Cartesian MRI. Different from the conventional MRI, where three spatially orthogonal gradient systems, namely x-, y-, and z-gradients, are used to control the magnetization precession frequency and to encode the spatial location via frequency analysis, PatLoc uses nonbijective curvilinear magnetic fields to achieve the goal of spatial encoding. Because the magnetization precession frequency/phase may not be uniquely encoded in a PatLoc system, parallel MRI has to combine with a PatLoc system to accurately localize the magnetization. Recently, prototypes of the PatLoc system have been successfully implemented on animal (5) and human scanners (6). So far, most PatLoc imaging has focused on using one pair of multipolar spatial encoding magnetic fields (SEMs) to encode spatial information (7–9). A reconstruction method has been presented in detail, which is fast because it allows the application of the traditional (fast) Fourier transform. Residual aliasing resulting from nonunique SEM encoding is resolved using methods of parallel image reconstruction. This, however, requires the explicit identification of the multiple locations, where SEM encoding is not unique. In generalized cases, this procedure can be computationally intensive or even prohibitive (9). In general, the magnetizations spatially encoded in a PatLoc system can, therefore, not use traditional (fast) Fourier transform to complete image reconstruction (9). This poses a computational challenge on reconstructing PatLoc images.

Even with the advantage of efficient image reconstruction, one caveat of using multipolar SEMs is the prominent loss of the spatial resolution at the center of FOV using a symmetric coil array. This is due to the circular symmetry of the multipolar SEMs and the reduced sensitivity of RF coils at the center of the FOV. Magnetization distribution around the center of the FOV is similarly encoded by both surface gradient elements and RF coils. This ambiguity leads to a highly ill-conditioned encoding and subsequently largely amplified noise around the FOV center.

The purpose of this study is (1) identifying multiple SEMs that can be realized by a generalized PatLoc

[1]Institute of Biomedical Engineering, National Taiwan University, Taipei, Taiwan.

[2]Harvard Medical School - Athinoula A. Martinos Center for Biomedical Imaging, Department of Radiology, Massachusetts General Hospital, Charlestown, Massachusetts, USA.

[3]Department of Radiology, University Medical Center Freiburg, Freiburg, Germany.

[4]Institute of Neuroscience, National Yang-Ming University, Taipei, Taiwan.

[5]Department of Biomedical Engineering and Environmental Sciences, National Tsing-Hua University, Hsinchu, Taiwan.

Part of this study has been presented in the previous Annual Meeting of International Society of Magnetic Resonance in Medicine (ISMRM), 2009.

Grant sponsor: United States National Institutes of Health (NIH, National Center for Research Resources); Grant numbers: R01HD040712, R01NS037462, R01NS048279, P41RR014075, R01MH083744, R21DC010060, R21EB007298; Grant sponsor: National Science Council, Taiwan; Grant numbers: NSC 98-2320-B-002-004-MY3, NSC 100-2325-B-002-046, 98-2517-S-004-001-MY3; Grant sponsor: National Health Research Institute, Taiwan; Grant number: NHRI-EX100-9715EC; Grant sponsor: Academy of Finland (FiDiPro Program); Grant number: 127624.

*Correspondence to: Fa-Hsuan Lin, Ph.D., Institute of Biomedical Engineering, National Taiwan University, Taipei, Taiwan. E-mail: fhlin@ntu.edu.tw or Fu-Nien Wang, Ph.D., Department of Biomedical Engineering and Environmental Sciences, National Tsing-Hua University, Hsinchu, Taiwan. E-mail: fnwang@mx.nthu.edu.tw

Received 16 March 2011; revised 18 October 2011; accepted 18 November 2011.

DOI 10.1002/mrm.24115

Published online 13 January 2012 in Wiley Online Library (wileyonlinelibrary.com).

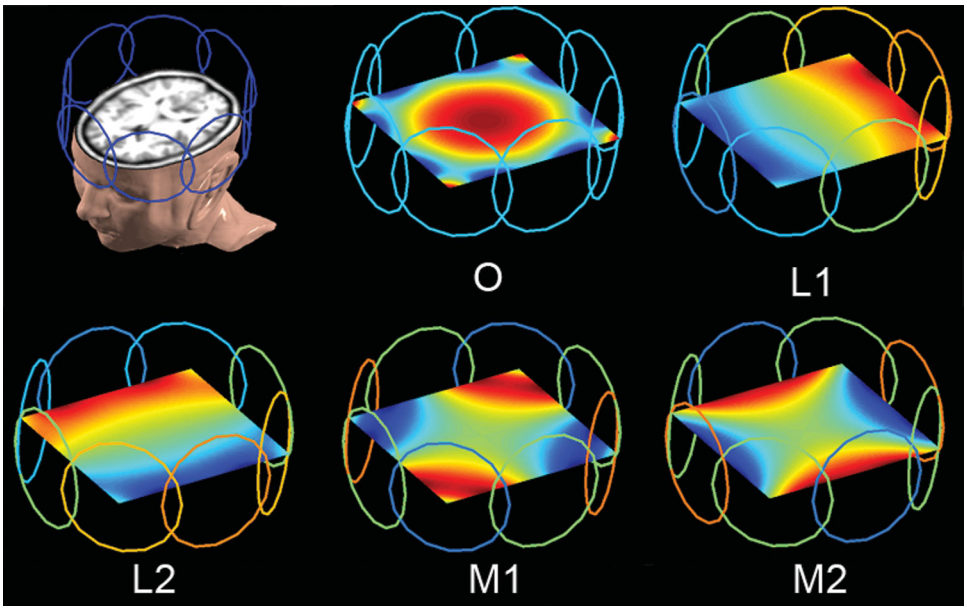


FIG. 1. The setup of an eight-channel PatLoc system (upper left). Using SVD, the five most significant SEMs suggested by singular value decomposition (SVD) on the magnetic fields generated by each channel of the PatLoc system are one O-space mode (O), two linear modes (L1 and L2), and two multipolar modes (M1 and M2). They constitute 42%, 21%, 21%, 6%, and 6% of the total variance, respectively. [Color figure can be viewed in the online issue, which is available at wileyonlinelibrary.com.]

system and (2) proposing a generalized PatLoc imaging encoding and reconstruction using multiple SEMs to reduce the loss of spatial resolution at the center of FOV without explicitly identifying the multiple locations of ambiguous SEM encoding. It has been shown that simultaneous switching of linear and multipolar SEMs can reduce the loss of spatial resolution around the FOV center (10,11). As described in the following section, we found that the present PatLoc coil could potentially generate not only the multipolar but also nearly linear SEMs. These SEMs are generated by driving a linear combination of PatLoc coil elements with current amplitudes and polarities suggested by singular value decomposition (SVD). Consecutive application of these two types of SEMs recovers the spatial resolution at the center of FOV. Practically, such an image reconstruction using multiple SEMs can be efficiently implemented by the conjugate gradient (CG) algorithm (12). Reconstructions using simulations and experimental data are compared with parallel MRI using conventional linear gradients to illustrate that the general combination of SEMs can improve image reconstructions.

## METHODS

### Signal Equation and SEMs

The PatLoc image reconstruction can be theoretically derived from the signal equation of a system using multiple surface gradient elements combined with the parallel detection across channels in a RF coil array (9):

$$\mathbf{s} = \mathbf{E}\rho, \qquad [1]$$

where $\mathbf{s}$ is a vector consisting of measurement across RF coil channels using individual SEMs with a particular driving current strength. and $\rho$ is the image to be reconstructed. Each row of the encoding matrix $\mathbf{E}$ represents a spatial basis function generated from the combination of one RF coil sensitivity profile and the time integral of a SEM generated from multiple gradient elements (9,10,13).

The simulations in this study used eight surface gradient elements with a circumferential geometry. Figure 1 shows the schematic plot of an eight-channel PatLoc system. The magnetic field generated by each gradient element was calculated using the Biot–Savart's law. Given eight magnetic fields generated by applying a unit current on each gradient element, we used SVD to propose different SEMs:

$$\mathrm{USV^H} = \mathrm{SVD(G)} = \mathrm{SVD([G_1\ G_2\ \ldots\ G_{nG}])},\ \mathrm{n_G} = 8, \qquad [2]$$

where $G_i$ is the spatial distribution of the z-component of the magnetic field generated by surface gradient element $i$ within the FOV in a column vector. The $p$th column of $\mathbf{V}$ suggests the driving currents for gradient elements to generate the $p$th SEM, whose spatial distribution is described by the $p$th column of $\mathbf{U}$. The $p$th diagonal entries of $\mathbf{S}$ indicate the relative proportion of the total variance with $[G_1\ G_2\ \ldots\ G_{nG}]$ by the $p$th SEM. Note that SVD ensures that different SEMs are orthogonal to each other across the FOV: $\mathbf{UU}^{\mathrm{H}} = \mathbf{I}_{n\mathrm{G}}$, where $\mathbf{I}_{n\mathrm{G}}$ is an identity matrix of dimension $n_{\mathrm{G}}$-by-$n_{\mathrm{G}}$. Locally, different SEMs are not necessarily orthogonal between each other. The top five SEMs suggested by SVD are shown in Fig. 1. Interestingly, SVD automatically suggested two multipolar SEMs used in previous PatLoc studies (4,9). These two are the fourth and fifth SEMs, each accounting for 6% of the total variance in $\mathbf{G}$. They are named the "M1" and "M2" SEMs, respectively, in this study. The second and third SEMs suggested by SVD have a nearly linear magnetic field spatial distribution in two orthogonal directions. Each SEM accounted for 21% of the total variance in $\mathbf{G}$ each. These two SEMs are named the "L1" and "L2" and were generated by driving surface gradient elements in a nearly sinusoidal distribution with a 90° shift. The isointensity contours of the magnetic field generated by the first SEM are concentric rings. This field has been used in the O-space imaging (14) and thus named the "O" SEM in this study.

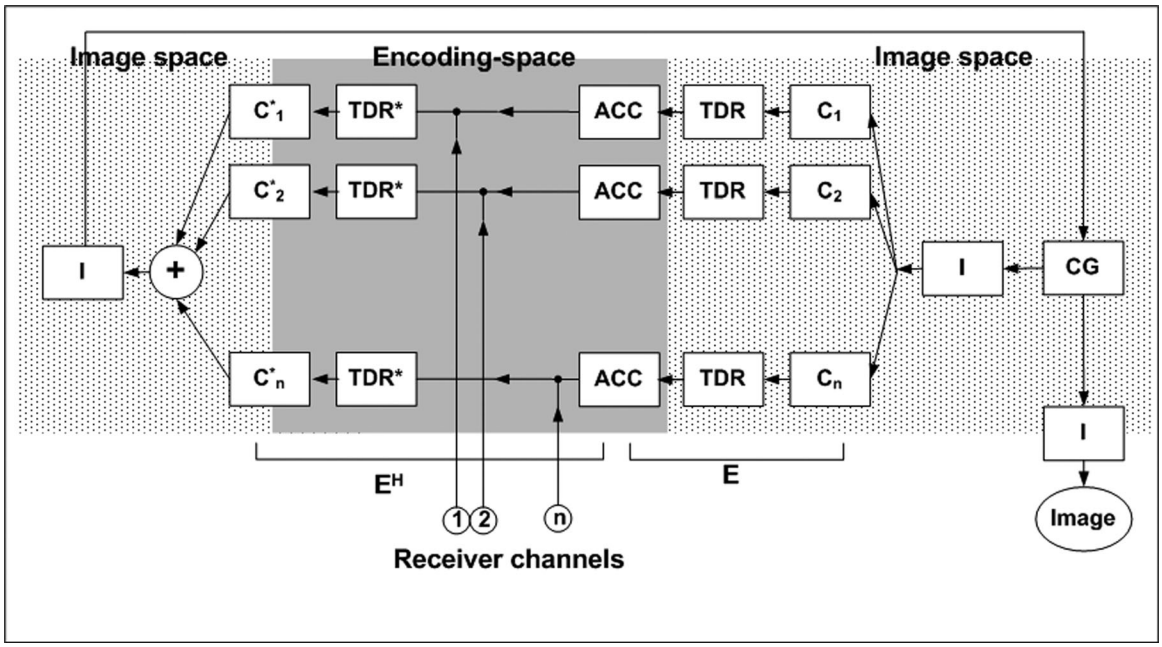


FIG. 2. The flow chart of the iterative time-domain reconstruction (iTDR) for PatLoc reconstruction with arbitrary configuration of the SEMs and data sampling scheme. ACC, encoding-space data subsampling; C, coil sensitivity modulation; TDR, the implementation of Eq. 1; CG, conjugate gradient algorithm; I, the intensity correction.

### Image Acquisitions and Reconstruction

One PatLoc imaging strategy is choosing a pair of SEMs and then drive these two SEMs, respectively, according to the "phase" and "frequency" encoding gradient time tables in a typical 2D MRI pulse sequence (or two orthogonal "phase" encoding gradients in a 3D acquisition) in a conventional MRI system (9). Thus, conventional imaging sequences can be used directly on a PatLoc system to acquire data. Considering a 2D PatLoc imaging case with two provided SEMs for phase encodings, encoded data can be mapped onto a two-dimensional encoding space similar to the 2D *k*-space in the Fourier imaging using linear gradients. As we attempted to accelerate PatLoc imaging, we subsampled the number of data in the *p*th SEM by reducing the data samples from $n_E(p)$ to $n_E^{ACC}(p)$. The acceleration $R$ was calculated by

$$R = \frac{\sum_{p=1}^{n_G} n_E(p)}{\sum_{p=1}^{n_G} n_E^{ACC}(p)} \quad [3]$$

Specifically, "L1" and "L2" SEMs were used together as the first pair of two phase encoding gradients in a 3D gradient echo sequence to collect $n_E(1)$ samples. "M1" and "M2" SEMs were used together as the second pair of two phase encoding gradients in a 3D gradient echo sequence to collect $n_E(2)$ samples. Without the loss of generality, here we only investigated cases $n_E(1) = n_E(2)$. In accelerated scans, we used the R1 × R2 acceleration rate to R1 × R2 acceleration to represent the accelerated acquisition of taking one sample from every consecutive R1 pixels in the first (phase) encoding dimension and one sample from every consecutive R2 pixels in the second (frequency) encoding dimension. The acquired data **s** from each pair of SEMs with corresponding spatial bases (rows of **E)** can be vertically concatenated as described in Eq. 1.

In this study, we investigated PatLoc imaging using (1) a pair of multipolar "M1" + "M2" SEMs and (2) two pairs of nearly linear "L1" + "L2" and multipolar "M1" + "M2" SEMs. Accelerated PatLoc acquisitions using aforementioned SEMs with 2-, 4-, and 8-fold accelerations were also simulated for image reconstruction. To fairly compare the reconstructed images subjected to the same acquisition time, the number of samples in acquisitions using multiple SEM pairs should be reduced compared with the acquisition using only one SEM pair. For example, using a 128 × 128 image matrix with 8-fold acceleration, PatLoc using only M1 + M2 SEMs collected 2048 samples. PatLoc using M1 + M2 + L1 + L2 SEMS collected 1024 samples from the pair of M1 + M2 SEMs and 1024 samples from the pair of L1 + L2 SEMs.

Because the Fourier transform can no longer be applied to solve Eq. 1 directly due to the fact that rows of **E** within each RF channel are not orthonormal in general, we propose an iterative time-domain reconstruction (iTDR) algorithm based on the CG method. The iTDR is a generalization of the sensitivity encoded (SENSE) image reconstruction with arbitrary *k*-space trajectories (12). One advantage of iTDR reconstruction is that it does not require defining locations of ambiguous SEM encoding a procedure required by the original PatLoc reconstructions (4,9). The algorithm is schematically depicted in Fig. 2, where **I** is the image intensity correction by dividing the input image with sum-of-squares of the coil sensitivity profiles in an RF coil array. $\mathbf{C}_i$ denotes the RF coil sensitivity profile for channel *i*, and ACC indicates

subsampling the *k*-space data based on the pulse sequence diagram. CG is the block of implementing the CG method by updating the reconstruction from the previous iteration. Note that the CG algorithm has been used in, for example, parallel MRI reconstruction (12). Here, we only used CG to solve the large linear system equation.

Simulations used high-resolution 3D $T_1$-weighted structural MRI data. The pulse sequence was magnetization prepared rapid gradient echo (MPRAGE) (pulse repetition time/echo time/flip = 2530 ms/3.49 ms/7°, partition thickness = 1.0 mm, matrix = 256 × 256, 256 partitions, and FOV = 256 mm × 256 mm). One axial slice image was selected as the input. We used the Biot–Savart's law to calculate the $B_1$ fields generated by an eight-channel head coil array with geometry similar to the PatLoc system depicted in Fig. 1. A sum-of-squares reference image from eight channels of the RF coil array was calculated after given $B_1$ fields. Simulations added Gaussian white noise with SNR = 1000 to avoid the overestimation of the reconstruction quality due to the exact match between the model and the noiseless synthetic measurements. The fidelity of the reconstruction was quantified by a difference image between the reference image and the sum-of-square image after reconstruction.

The spatial resolution of the reconstructed images was evaluated by the point-spread functions (PSFs). Specifically, an image with all pixels with intensity zero except a center pixel or a pixel close to the periphery of the FOV set to one was used as the input image. The reconstructed image was the corresponding empirical PSF of the input image. We quantified the PSF by measuring its full-width-half-maximum (FWHM). Recently, the concept of local *k*-space has been proposed to examine the spatial resolution in PatLoc imaging (13). Similar to conventional MRI, *k*-space coordinates can be derived as the local partial spatial derivative of the phase generated by given SEM strength and duration $k(p,q)$ at location $\vec{r}$:

$$\begin{aligned} k_x(q,\bar{r}) &= \frac{\partial}{\partial x} - j2\pi\gamma \sum_{p=1}^{n_G} [k(p,q)\mathrm{SEM}(p,\bar{r})], \\ k_x(q,\bar{r}) &= \frac{\partial}{\partial y} - j2\pi\gamma \sum_{p=1}^{n_G} [k(p,q)\mathrm{SEM}(p,\bar{r})], \end{aligned} \quad [4]$$

where $p$ denotes the index for different SEM, and $q$ denotes the index of the acquisition data for different time integral of the SEM. However, different from conventional MRI, because we have nonlinear SEMs in general, the *k*-space is not identical across the FOV. Thus, it gives the name "local *k*-space" to highlight the spatial varying nature of Eq. 4.

We calculated the local *k*-space to visualize the variable spatial resolution at different image voxels. All calculations were implemented with MatLab (Mathworks, Natick, MA) on a workstation with Intel 2.0 GHz Xeon CPU and 32 GB memory.

PatLoc imaging data using linear and multipolar SEMs were acquired on a 3-T clinical imaging system (Tim Trio, Siemens Healthcare, Erlangen, Germany) fitted with a custom-built gradient insert coil designed to generate two encoding fields. The geometry of each multipolar SEM closely approximates a hyperbolic paraboloid, generating two locally orthogonal SEMs rotated by 45° with respect to each other. Details of the PatLoc arrangement have been previously described in Refs. 6 and 15. A head coil was fitted inside the gradient insert and consisted of a single-channel transmitter and an eight-channel receive array (Siemens Healthcare, Erlangen, Germany). Data using only traditional linear gradients and two multipolar SEMs were acquired separately. Imaging parameters were as follows: FOV = 220 mm, image matrix = 256 × 256, slice thickness = 5 mm, pulse repetition time = 50 ms, and echo time = 8.1 ms.

## RESULTS

Provided with SEMs and the acquisition grids, we directly reconstructed images without explicit determination of the locations encoded ambiguously with the SEMs using the iTDR. Figure 3 shows the convergence behaviors of the PatLoc reconstructions using only multipolar SEMs (M1 + M2) and using the combination of multipolar and nearly linear SEMs (M1 + M2 + L1 + L2). Provided with the reference image in the synthetic data, we calculated the percentage error of the reconstruction at each repetition. Over the first 10 iterations, the percentage error dropped over 80% using either M1 + M2 or M1 + M2 + L1 + L2 SEMs. The convergence rates for different accelerated data were different: a higher acceleration rate corresponded to a slower convergence. This can be explained by the deteriorated conditioning of the encoding matrix (Eq. 1) in more accelerated acquisitions. We found that the reconstruction converged after 50 iterations. For acquisitions without acceleration ($R = 1 \times 1$), with 2-fold ($R = 2 \times 1$) and 4-fold ($R = 2 \times 2$) accelerations, the final reconstruction has the percentage error less than 5%. Eight-fold acceleration ($R = 2 \times 4$) converged at 5 and 3% error using M1 + M2 and M1 + M2 + L1 + L2 SEMs, respectively.

Figure 4 shows the reconstructed images and the corresponding error images at different iterations without acceleration and with 8-fold ($R = 2 \times 4$) accelerations. For comparison, results using M1 + M2 SEMs and M1 + M2 + L1 + L2 SEMs were shown together. Starting from a zero image, the reconstruction started from the center of the FOV during the first few repetitions. These images corroborated with the convergence plots shown in Fig. 3: a higher acceleration rate converged more slowly. The final reconstructed images without acceleration had a percentage error of 1% and with 8-fold accelerations the reconstruction had percentage errors of 5 and 3% using M1 + M2 SEMs and M1 + M2 + L1 + L2 SEMs, respectively.

Details of the final reconstructions are shown in Fig. 5. For comparison, we also showed the reference images and the reconstruction using conventional linear gradients. Without acceleration (Fig. 5, top row), we found that all reconstructions around cortex were satisfactory. Minor reconstruction error (<1%) was due to the simulated noise. However, at the center of the FOV, the PatLoc reconstruction using only M1 + M2 was blurred. Such a loss of spatial resolution at the center of the image (indicated by a yellow arrow head) was consistent with previous studies (4,9): SEMs and coil sensitivity

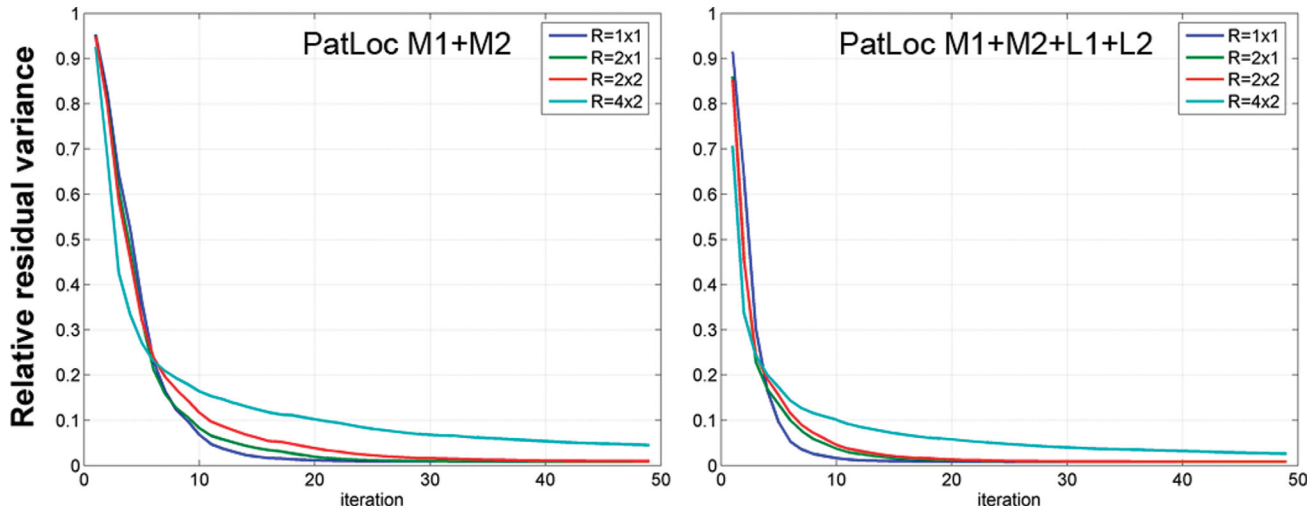


FIG. 3. The convergence of the iTDR PatLoc reconstructions using M1 + M2 SEM (left) and M1 + M2 + L1 + L2 SEM (right) with $R = 1 \times 1$, $R = 2 \times 1$, $R = 2 \times 2$, and $R = 2 \times 4$ accelerations. Convergent reconstructions were found after 50 iterations in general. [Color figure can be viewed in the online issue, which is available at wileyonlinelibrary.com.]

maps from a coil array cannot provide sufficient spatial information to reliably resolve images in the FOV center. Note that by using the L1 and L2 SEMs in conjunction with the M1 and M2 SEMs, we improved the loss of the spatial resolution around the FOV center significantly. The reconstruction was found similar to the one from using the conventional linear gradient system over the FOV uniformly.

Accelerated reconstructions are also shown in Fig. 5. At 4-fold acceleration ($R = 2 \times 2$), PatLoc reconstruction with multipolar SEMs (M1 + M2) still have prominent loss of spatial information at the FOV center (yellow arrow heads). Using linear gradient system or PatLoc with multipolar and nearly linear SEMs generated comparable reconstructions to the reference image (Fig. 5, middle row). The noise level of the reconstruction was found marginally higher in the 4-fold accelerated case (0.9%) than the unaccelerated case (0.8%), potentially due to the 50% reduction on the sample and/or the noise amplification during the reconstruction. Eight-fold acceleration showed clear differences among reconstructions (Fig. 5, bottom row). As this PatLoc system has eight RF coils, the maximal acceleration rate was eight before transforming the signal equation (Eq. 1) from an overdetermined linear system into an underdetermined linear system. Using the linear gradient system, clear residual aliasing artifact along the left–right direction was found in the $2 \times 4$ acceleration (green arrow heads). PatLoc reconstructions using only multipolar SEMs (M1 + M2) showed the loss of spatial information at the FOV center (yellow arrow heads) and noisy reconstruction at the frontal and occipital areas (magenta arrow heads). With M1, M2, L1, and L2 SEMs, the 8-fold reconstructed PatLoc image showed less aliasing artifact than the linear gradient reconstruction, improved spatial resolution in the FOV center, and reduced noise level in the frontal and occipital lobes.

Because conventional MRI readily provides highly linear gradient coils, we wondered how reconstructions change if we replace the L1 + L2 SEMs generated by the PatLoc system with the two linear $B_z$ (linear 1 + linear 2) generated by the conventional MRI gradient coils. Figure 6 shows such comparison without acceleration and with 4-fold and 8-fold accelerations ($R = 2 \times 2$ and $R = 2 \times 4$). We found that reconstructions using either L1 + L2 or linear 1 + linear 2 are pretty similar at $R = 1$ and $R = 2 \times 2$. At a high acceleration rate $R = 2 \times 4$, the reconstruction noise was more prominent using the linear $B_z$. This might be due to the difficulty of using the RF sensitivities to interpolate the missing spatial bases generated by linear $B_z$.

Figure 7 shows the reconstructions of different SNR at $R = 2 \times 2$ and $R = 2 \times 8$. We can see that at a fixed acceleration rate, the reconstruction deteriorated as the SNR decreased. Notably, at SNR = 100, $R = 2 \times 2$ shows fairly good reconstruction (residual error = 0.3%). At $R = 2 \times 4$, the reconstruction shows noticeable noises at SNR = 100 (residual error = 3.4%). We consider that the reconstruction can work satisfactorily at SNR = 100 or higher.

The proposed iTDR reconstruction has the capability of reconstructing images using arbitrary SEMs. Figure 8 shows an example of using two SEMs generated by randomly weighting the surface gradient elements. In this example, details of images can be restored in lower left corner of the FOV based on sufficient spatial information from the highly nonlinear SEM pairs and RF coil sensitivities.

To evaluate the spatial resolution, PSFs corresponding to a pixel at the FOV center and the peripheral of the FOV are shown in Fig. 9. The locations of the nonzero image pixel for the PSF input image are surrounded by cyan boxes and indicated by cyan arrow heads. Although the PSF at the FOV periphery was very focal, we found that the center of FOV has a spatially blurred PSF when only M1 + M2 SEMs were used. Using L1 + L2 SEMs and M1 + M2 SEMs, the PSF at the FOV periphery can maintain focal, and the PSF at the FOV center can be improved clearly by suppressing side lobes. The bottom panel of Fig. 7 plots the profile of the PSF along a vertical line passing through the nonzero pixel in the PSF input image. The location of the nonzero input PSF

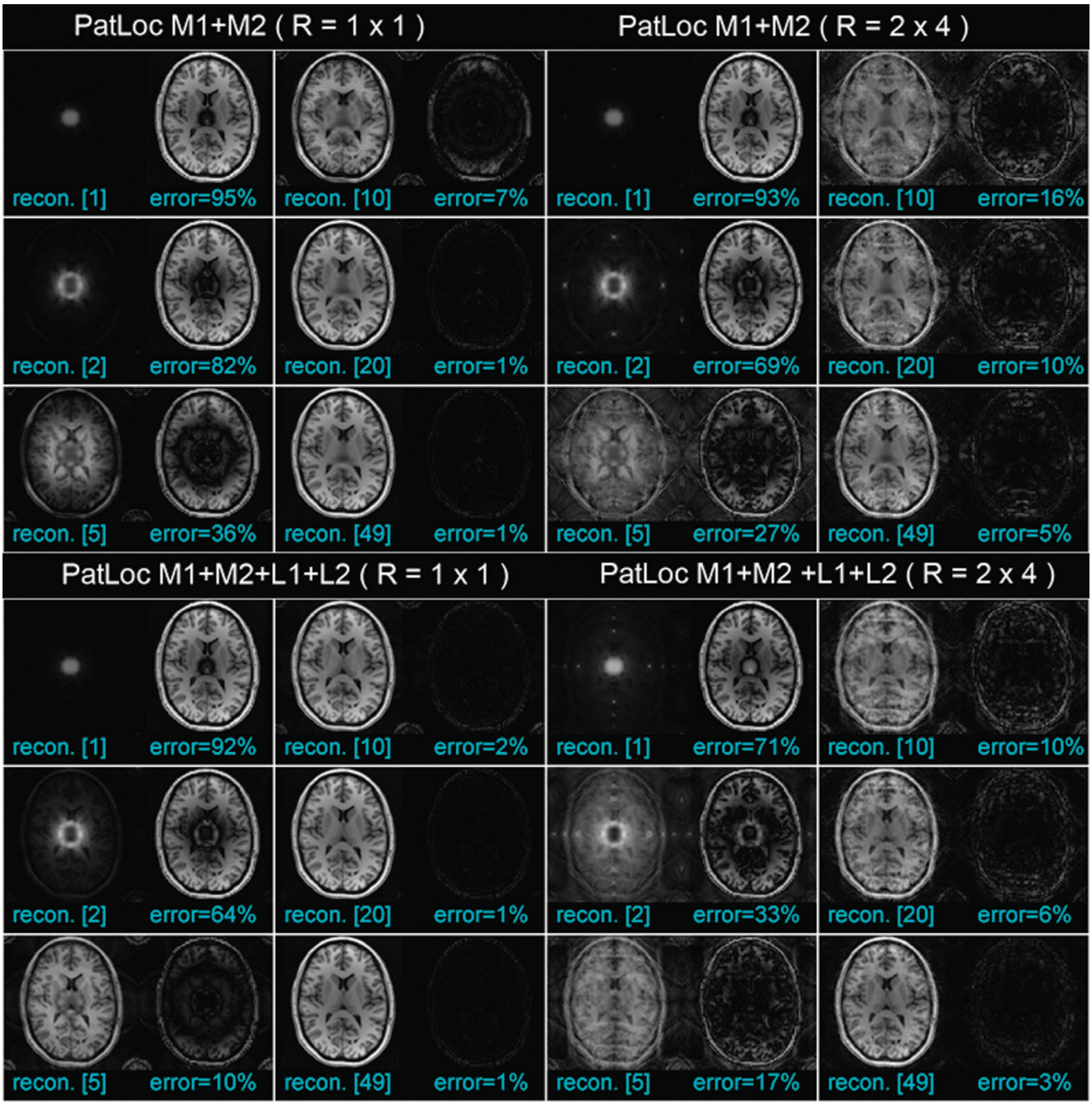


FIG. 4. Individual reconstructed images and error images using iterative time-domain reconstruction (iTDR). Each subplot shows the reconstruction (left) and the residual error image (right) in each repetition. At a higher acceleration rate, the convergence was slower. [Color figure can be viewed in the online issue, which is available at wileyonlinelibrary.com.]

image is indicated by a gray dashed line. Quantitatively, the FWHMs at FOV periphery using M1 + M2 SEMs and M1 + M2 + L1 + L2 SEMs were both 1.0 pixel. The FWHMs at FOV center using M1 + M2 SEMs and M1 + M2 + L1 + L2 SEMs were 7.0 and 2.2 pixels, respectively. We also found that the peak of the center FOV PSF shifted by 2 pixels when only M1 + M2 SEMs were used.

PSFs were also evaluated for reconstructions using the accelerated data. Figure 10 plots the profiles of the PSFs for input images with a nonzero pixel at the FOV center (Fig. 10, left) and at the FOV periphery (Fig. 10, right). We found that acceleration modulated the PSF marginally. Using only multipolar SEMs, the PSFs at the FOV center were blurred with FWHMs of 7.0 pixels, 7.4 pixels, and 7.8 pixels for $R = 1 \times 1$, $R = 2 \times 2$, and $R = 2 \times 4$, respectively. The peak of the PSF was also found shifted by 2 pixels for all acquisitions. Using multipolar and linear SEMs, the PSFs at the FOV center were much focal with FWHMs of 2.2 pixels, 2.3 pixels, and 2.4 pixels for $R = 1 \times 1$, $R = 2 \times 2$, and $R = 2 \times 4$, respectively. At the FOV periphery, all reconstructions using either M1 + M2 SEMs or M1 + M2 + L1 + L2 SEMs had a PSF of 1.0 pixel for unaccelerated ($R = 1 \times 1$) and accelerated ($R = 2 \times 2$ and $R = 2 \times 4$) acquisitions.

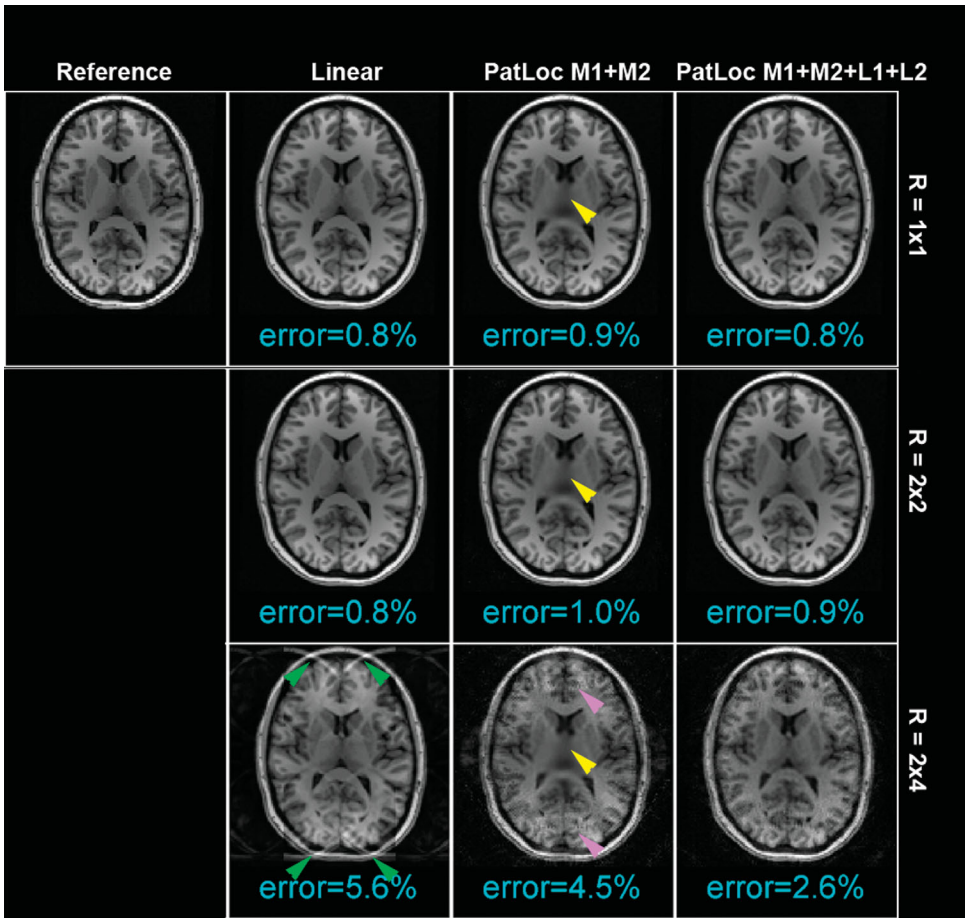


FIG. 5. Reconstructed images using conventional linear gradient coils and PatLoc system with multipolar (M1 + M2) SEMs and with multipolar as well as linear (M1 + M2 + L1 + L2) SEMs. Reconstructions using unaccelerated acquisitions ($R = 1 \times 1$), 4-fold acceleration ($R = 2 \times 2$), and 8-fold acceleration ($R = 2 \times 4$) are shown in the top, middle, and bottom rows, respectively. PatLoc using M1 + M2 SEMs shows reduced image resolution at the FOV center (yellow arrow heads). At 8-fold acceleration, conventional linear gradients generate strong aliasing artifacts at 8-fold acceleration (green arrow heads) and PatLoc with M1 + M2 SEMs shows noisy reconstructions at the frontal and occipital lobes (magenta arrow heads). PatLoc with M1 + M2 + L1 + L2 SEMs has comparably better image quality. [Color figure can be viewed in the online issue, which is available at wileyonlinelibrary.com.]

The spatial resolution analysis using PSF corroborates the local *k*-space analysis. Figure 11 shows that the local *k*-space at $7 \times 7$ image voxels evenly distributed over the FOV. Using only multipolar SEMs has a low spatial resolution around the FOV center, consistent with previous studies (13). FOV periphery does not lose spatial resolution. These local *k*-space calculations are consistent with the PSF calculations (Figs. 9 and 10). Using both multipolar and nearly linear SEMs, the local *k*-space shows improved spatial resolution around the FOV center as the result of increased *k*-space coverage. From the local *k*-space plot, it is evident that the corresponding local *k*-space distribution is the sum of local *k*-space using individual SEMs, as also described in Eq. 4.

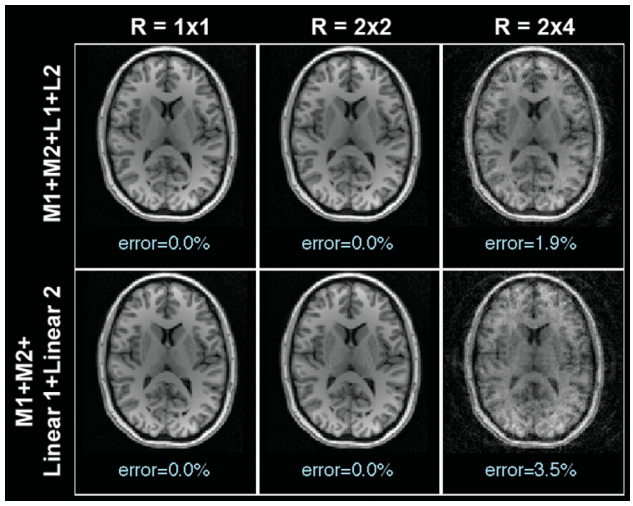


FIG. 6. PatLoc imaging reconstructions using the multipolar (M1 + M2) SEMs and the nearly linear (L1 + L2) SEMs generated by the PatLoc system or the multipolar (M1 + M2) SEMs together with the two linear (linear 1 + linear 2) $B_z$ fields generated by the conventional gradient coils. [Color figure can be viewed in the online issue, which is available at wileyonlinelibrary.com.]

Experimental reconstructions using data with linear gradients, multipolar SEMs (M1 + M2), and four SEMs together are shown in Fig. 12. As limited by currently available hardware, the linear gradients were generated from the linear gradient coils in the conventional MRI system. Because our calculation (Fig. 6) shows little difference between reconstructions using nearly linear SEMs generated by the generalized PatLoc system and the linear gradients generated by the conventional MRI gradient coils, we considered Fig. 12 is what can be achieved using L1/L2 and M1/M2 SEMs by the PatLoc system. Compared with reconstruction using only multipolar SEM acquisitions, the loss of spatial resolution around the FOV center was reduced when four SEMs were used together. However, we noticed that around the FOV center the spatial resolution was not recovered completely. There were also more prominent residual aliasing artifacts when four SEMs were used. Similar to a recently published study (13), this suboptimal

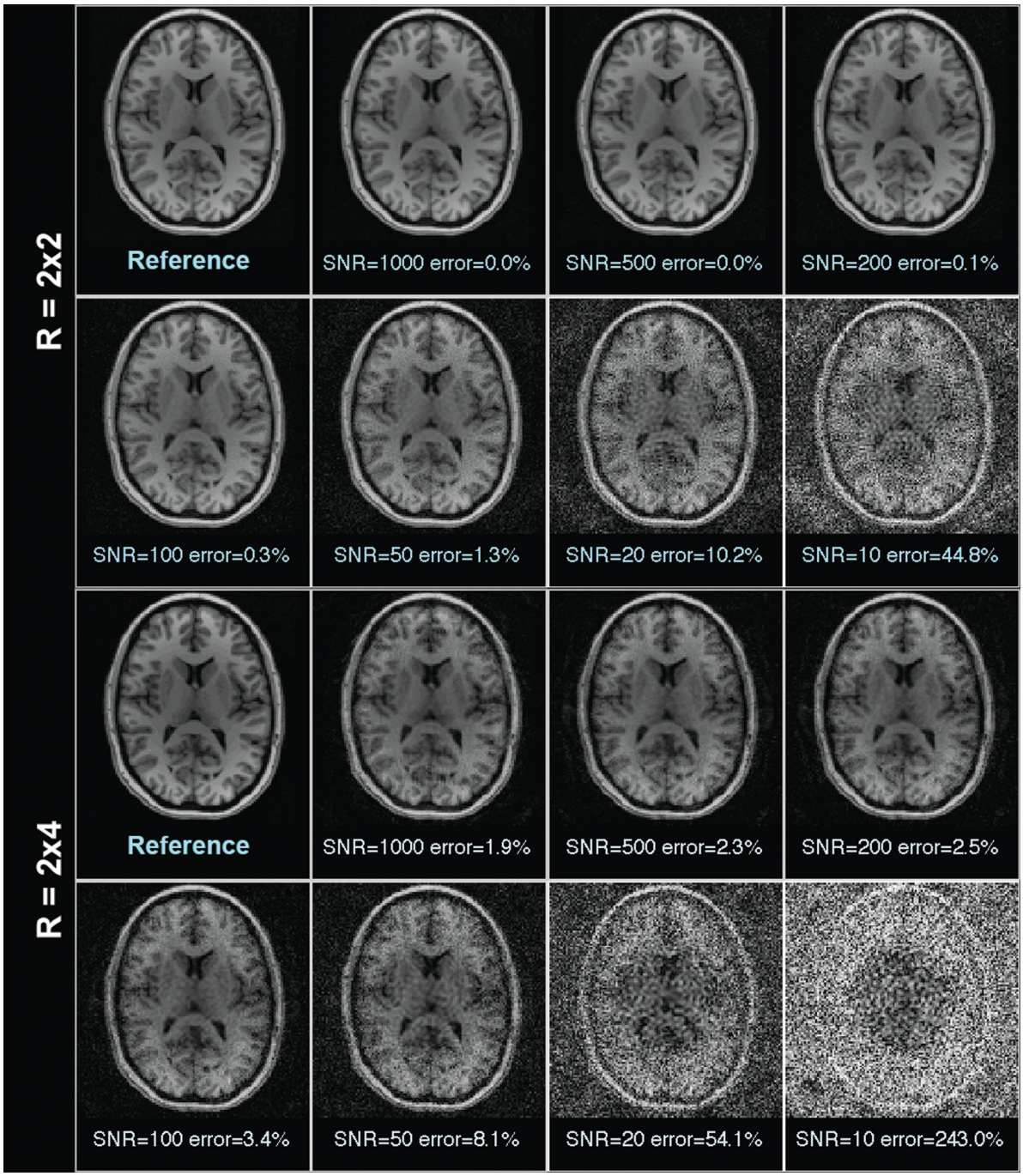


FIG. 7. Accelerated ($R = 2 \times 2$ and $R = 2 \times 4$) PatLoc imaging reconstructions using the multipolar (M1 + M2) and the nearly linear (L1 + L2) SEMs at SNR = 1000, 500, 200, 100, 50, 20, and 10. [Color figure can be viewed in the online issue, which is available at wileyonlinelibrary.com.]

performance is likely due to errors in the estimation of multipolar SEMs and RF coil sensitivity maps. For example, the coil sensitivity maps were estimated from a separate reference scan. Even though such a method ensured consistent coil loading such that estimated coil sensitivity is consistent between the reference scan and PatLoc imaging scan, motion between two scans as well as different eddy current effects can lead to inaccurate coil sensitivity estimation and cause imperfect reconstruction.

## DISCUSSION

This study addresses two challenges of the PatLoc imaging. First, we proposed the PatLoc acquisitions using multiple (potentially arbitrary) SEMs and a generalized image reconstruction algorithm without explicitly defining the locations identically encoded by the SEMs. Although we only demonstrated the iTDR reconstructions using multipolar and nearly linear SEMs, the same algorithm can be applied to different SEMs directly (Fig.

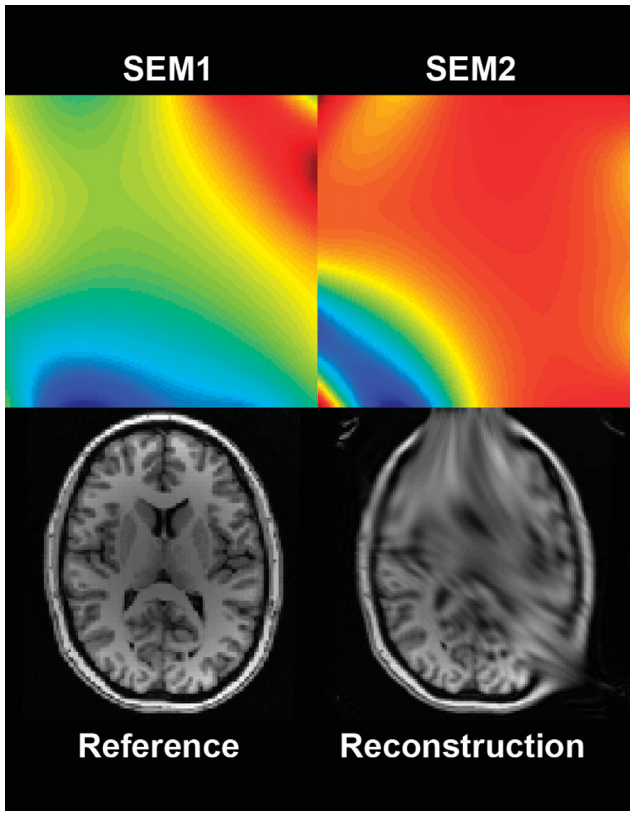


FIG. 8. iTDR can reconstruct images using arbitrary SEMs. Two SEMs generated by randomly weighting the gradient elements are shown at top. A reference image (bottom left) encoded by these two SEMs and iTDR reconstructs the highly distorted image (bottom right) efficiently. [Color figure can be viewed in the online issue, which is available at wileyonlinelibrary.com.]

8). Second, we investigated different SEMs that can be generated from a given PatLoc system. Importantly, two nearly linear SEMs were revealed via SVD. Previously, using multipolar SEMs alone, the reconstructed image has a poor spatial resolution at the center of FOV, where the spatial information from the RF coil sensitivity profiles and SEMs are insufficient to localize precession magnetization accurately (4,9). This challenge was mitigated by using multipolar and linear SEMs together, as demonstrated in Figs. 4 and 5. For unaccelerated image acquisitions, the image was found much improved in the FOV center. For accelerated acquisitions, PatLoc reconstructions using multipolar and linear SEMs have less aliasing artifact than using acquisitions in a linear gradient system and reduced noise compared with using multipolar SEMs only.

It should be noted that the realized PatLoc system is different from our simulation setup, as we do not currently have hardware in place to drive all eight elements of the PatLoc insert coil independently. However, our simulation is still valid as this setup has been used in the original PatLoc study showing good agreement between the simulations and experimental data (4). The SEMs are also quasi-static magnetic fields, and thus Biot–Savart's law can be used to generate reasonable field patterns. Different practical designs have been described in Refs. 9,13, and 16–18.

Via SVD, we found that nearly linear SEMs can be generated from the linear combination of surface gradient elements directly without using the conventional linear gradient coils. Considering multiple surface gradient elements arranged circumferentially with a uniform spacing, driving these elements with current amplitudes following a single cycle sinusoid pattern can generate fairly linear SEMs. Even though the current imaging hardware may not have this capability, our results suggest that a PatLoc system without traditional linear gradients can actually do all imaging experiments in a conventional MRI system depending on linear gradients coils. Because linear gradient coils can be theoretically replaced by PatLoc linear SEMs, a wider bore size, for example, compared with the existing PatLoc system is possible if the surface gradient elements can be as powerful and efficient as the whole-body gradient system. It should be noted that the PatLoc coil used in our experiments was hardwired to produce the multipolar M1- and M2-fields (Fig. 1) only. Technical realization of a freely configurable array of eight independent coil elements may be challenging in terms of equipment setup, eddy current behavior, and mechanical stabilization.

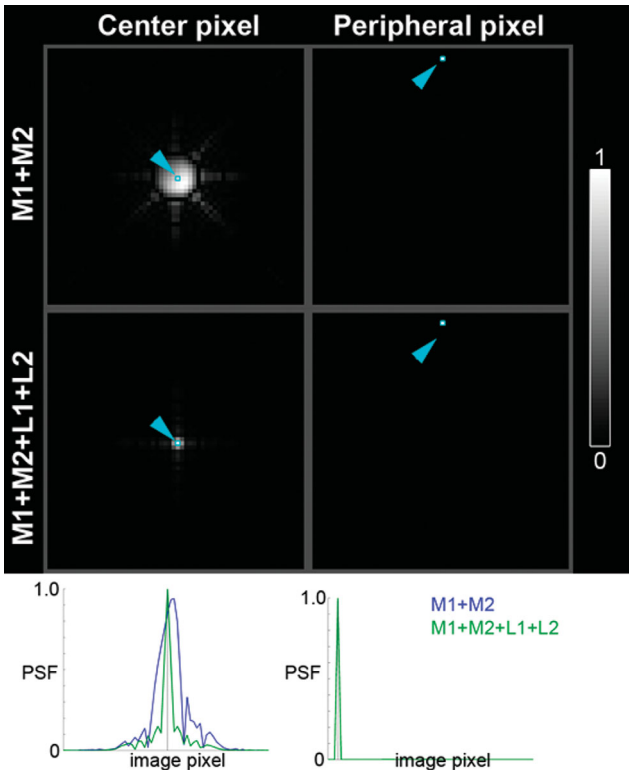


FIG. 9. The point-spread function (PSF) at the center of the FOV (left column) and the periphery of the FOV (right column) for unaccelerated PatLoc imaging using either multipolar (M1 + M2) or multipolar and linear (M1 + M2 + L1 + L2) SEMs. The cyan boxes and cyan arrow heads indicate the location of the nonzero input image pixel in PSF evaluation. The bottom panel shows the profile of the PSF along a vertical line passing through the nonzero PSF input image pixel. The gray dashed line indicates the location of the nonzero PSF input image pixel. [Color figure can be viewed in the online issue, which is available at wileyonlinelibrary.com.]

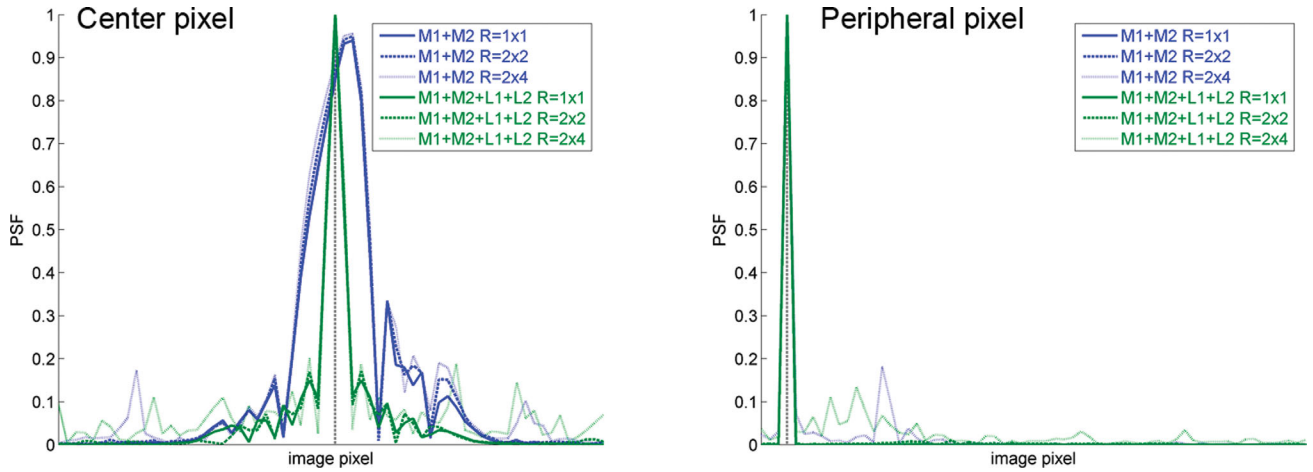


FIG. 10. The point-spread function (PSF) at the center of the FOV (left) and the periphery of the FOV (right) for unaccelerated ($R = 1 \times 1$) and accelerated ($R = 2 \times 2$ and $R = 2 \times 4$) PatLoc imaging using either multipolar (M1 + M2) or multipolar and linear (M1 + M2 + L1 + L2) SEMs. The gray dashed line indicates the location of the nonzero PSF input image pixel. [Color figure can be viewed in the online issue, which is available at wileyonlinelibrary.com.]

SVD on the collection of $B_z$ from all surface gradient elements revealed not only multipolar and linear SEMs but also the O-ring SEM and other configurations (Fig. 3). Notably, the O-ring SEM corresponded to the most significant singular value/vector (42% of the total variance). However, we want to clarify that singular values and the associated singular vectors here are not directly related to the spatial resolution or the reconstruction efficiency of PatLoc imaging. In fact, the spatial bases used for PatLoc imaging are spatially dependent complex sinusoids with phases proportional to the temporal integral of SEMs. The "O" SEM was indeed the SEM used in O-space imaging (14). In fact, the implementation of O-space imaging uses not only the "O" SEM but also the linear SEMs offered by the conventional imaging gradients to make different center placements. As the generalized PatLoc system can have the capability of generating nearly linear SEMs, O-space imaging can be implemented on a PatLoc system. The encoding fields from previous PatLoc and O-space implementations are, thus, theoretically related to each other by using different SEMs generated from a system of surface gradient elements with a circumferential arrangement. Although we did not explore including O-ring SEM for PatLoc imaging here, some preliminary studies have suggested that different SEMs, including O-ring, M1/M2, and L1/L2 SEMs, can be used jointly to improve the spatial

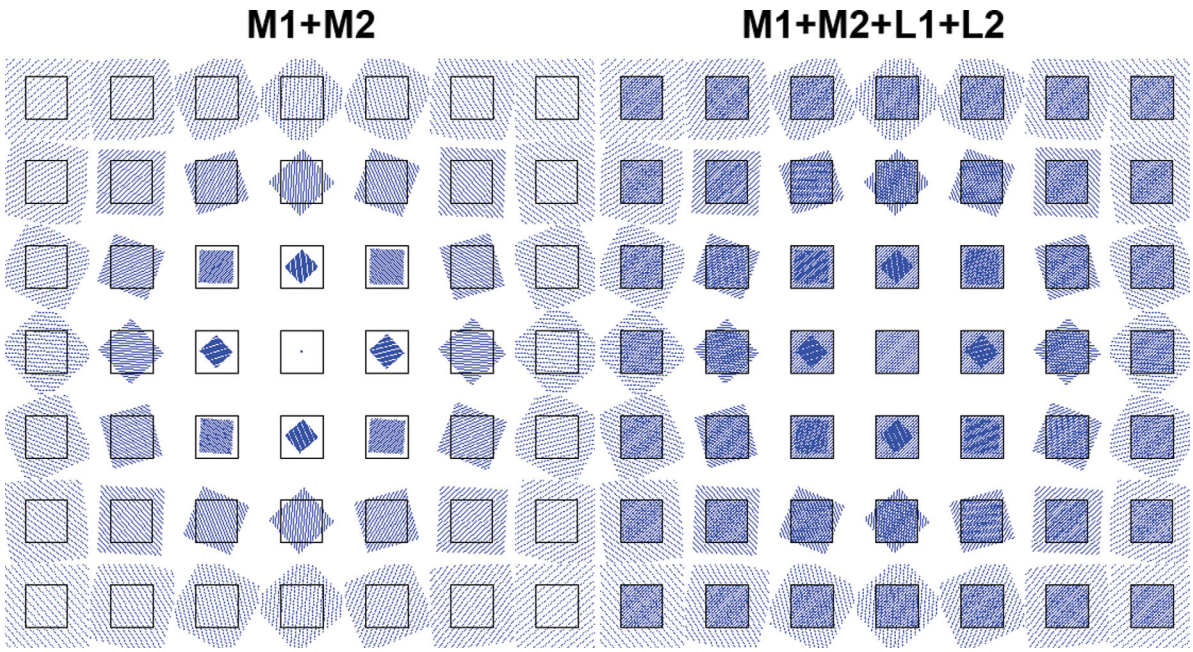


FIG. 11. The local *k*-space for unaccelerated PatLoc imaging using either multipolar (M1 + M2) or multipolar and linear (M1 + M2 + L1 + L2) SEMs. Improved spatial resolution around the FOV center was observed using four SEMs due to a wider *k*-space coverage. [Color figure can be viewed in the online issue, which is available at wileyonlinelibrary.com.]

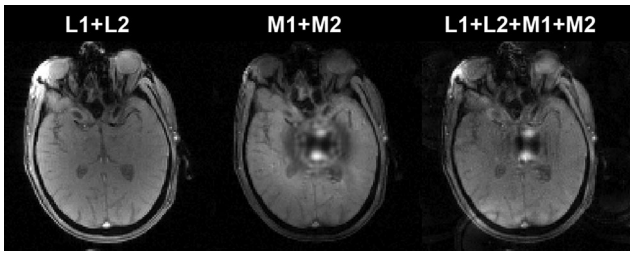


FIG. 12. Reconstructions of experimental images acquired using linear gradients (L1 + L2), multipolar PatLoc SEMs (M1 + M2), and the combination of four SEMs (L1 + L2 + M1 + M2).

encoding efficiency (19). We will pursue this research topic in the near future.

Generating nearly linear SEMs is the outcome of a PatLoc system with eight surface gradient elements in a symmetric arrangement. Other hardware configurations may not be able to generate nearly linear SEMs. In cases where nearly linear SEMs were not available, it is possible to use the linear gradient coils readily in the conventional MRI system together with the PatLoc SEMs to reduce the spatial resolution loss at the FOV center when the interactions between two systems have been considered carefully. This was demonstrated in Fig. 6.

This study investigated accelerated image acquisitions and reconstructions using PatLoc SEMs (Figs. 4 and 5). However, defining acceleration factor for nonlinear encoding can be more complicated than just simply controlling the data acquisition time. Specifically, fair comparisons between accelerated and unaccelerated data become difficult due to the varying spatial resolution across the FOV. Although the number of samples was kept the same across all encoding schemes, the effective local resolution was different. For example, acceleration could be achieved by acquiring fully sampled low-resolution artifact-free images. Yet, accelerated PatLoc images may be complicated by residual aliasing artifacts. Related to the heterogeneous spatial resolution in PatLoc, the percentage error reported in this study depended on the object used for simulation. If the object had fairly low spatial resolution, then the errors would remain low.

The results reported in this study can be further generalized in a few directions. First, the acquisition grid was only limited to the uniform sampling case. It is possible to adopt sampling patterns with spatially heterogeneous density in the encoding space. Considering natural images with dominant low spatial frequency components in general, it is reasonable to oversample the encoding space corresponding to spatial bases showing slow spatial variability to obtain better results. The iTDR reconstruction immediately allows such image reconstructions. This is different from reconstruction based on the fast Fourier transform, which usually requires data samples separated by equal spacing in the encoding space. The iTDR reconstruction can avoid the necessary regridding procedure from a non-Cartesian grid to a Cartesian grid and, in theory, calculate the reconstruction from arbitrary sampling patterns.

Encoding using nearly linear and multipolar SEMs can be realized in different approaches. This study proposed the acquisitions of using multipolar SEM pair and nearly linear SEM pair separately. Note that it has been recently suggested that multipolar and linear SEMs can be simultaneously turned on to achieve similar results of a more homogeneous spatial resolution (13). Differently, the approach suggested in this study is to turn on multipolar and linear SEMs consecutively. Here, we only investigated the case where samples from each multipolar and linear SEM pairs constitute 50% of the total data samples. It is possible to release from such a constraint that different SEM pairs acquire different proportions of samples such that the acquisition and the reconstruction can be further optimized.

Even though we used SVD to reveal combinations of driving currents on the surface gradient elements to generate SEMs, it is important to notice that using alternative decompositions can reveal other potentially interesting SEMs. SVD ensures that different SEMs are globally orthogonal with each other. Such an othogonality condition, in fact, may not be required in the generalized MRI using nonlinear SEMs. Elucidating the optimal SEMs remains an open question.

In this study, we spatially encode the object by pairs of SEMs. Provided with $n_{\mathrm{SEM}}$ SEMs, there exists $n_{\mathrm{SEM}}(n_{\mathrm{SEM}} - 1)/2$ choices of SEM pairs, each of which can manipulate its strength to acquire a data sample onto a 2D encoding space. More generally, it is actually possible to modulate the strength of $n_{\mathrm{SEM}}$ SEMs simultaneously. This is effectively encoding an object onto an $n_{\mathrm{SEM}}$-dimensional encoding space. Such an increase in the encoding dimensionality brings more degrees of freedom in the spatial basis functions generated from the conjunction of gradient elements and RF coil. Hypothetically, we may more efficiently encode the object: images can be more accurately described using fewer spatial bases. This will be further investigated in the near future.

PatLoc potentially can be used in applications where a high slew rate is needed with reduced nerve stimulation hazard (4). Additionally, it has been shown that PatLoc system can be used to achieve small FOV imaging (20) and parallel transmission (21,22). However, the price to pay includes the complexity in hardware availability, control, and image reconstruction. Advantages and disadvantages should be traded-off by considering the nature of different MR experiments.

## ACKNOWLEDGMENTS

The authors acknowledge Anna Masako Welz and Chris A. Cocosco for their contribution to the experimental setup in Freiburg and support of in vivo measurements.

## REFERENCES

1. Roemer PB, Edelstein WA, Hayes CE, Souza SP, Mueller OM. The NMR phased array. Magn Reson Med 1990;16:192–225.
2. Sodickson DK, Manning WJ. Simultaneous acquisition of spatial harmonics (SMASH): fast imaging with radiofrequency coil arrays. Magn Reson Med 1997;38:591–603.
3. Pruessmann KP, Weiger M, Scheidegger MB, Boesiger P. SENSE: sensitivity encoding for fast MRI. Magn Reson Med 1999;42:952–962.
4. Hennig J, Welz AM, Schultz G, Korvink J, Liu Z, Speck O, Zaitsev M. Parallel imaging in non-bijective, curvilinear magnetic field gradients: a concept study. MAGMA 2008;21:5–14.

5. Welz AM, Zaitsev M, Lehr H, Schultz G, Liu Z, Jia F, Post H, Korvink J, Hennig J.Initial realisation of a multichannel, non-linear PatLoc gradient coil. In: Proceedings of the International Society of Magnetic Resonance in Medicine, Toronto, Ontario, Canada, 2008. p. 1163.
6. Cocosco C, Dewdney A, Dietz P, Semmler M, Welz A, Gallichan D, Weber H, Schultz G, Hennig J, Zaitsev M.Safety considerations for a PatLoc gradient insert coil for human head imaging. In: Proceedings of the International Society of Magnetic Resonance in Medicine, Stockholm, Sweden, 2010. p. 3946.
7. Schultz G, Zaitsev M, Hennig J.Effects of discrete and finite sampling in PatLoc imaging. In: Proceedings of the International Society of Magnetic Resonance in Medicine, Honolulu, HI, 2009. p. 563.
8. Schultz G, Welz A, Hennig J, Zaitsev M.Generalized two-dimensional orthogonal spatial encoding fields. In: Proceedings of the International Society of Magnetic Resonance in Medicine, Toronto, Ontario, Canada, 2008. p. 2992.
9. Schultz G, Ullmann P, Lehr H, Welz AM, Hennig J, Zaitsev M. Reconstruction of MRI data encoded with arbitrarily shaped, curvilinear, nonbijective magnetic fields. Magn Reson Med 2010;64: 1390–1403.
10. Lin F-H, Witzel T, Polimeni J, Hennig J, Schultz G, Belliveau JW, Wald LL.Parallel imaging technique using localized gradients (PatLoc) reconstruction using orthogonal mode decomposition. In: Proceedings of the International Society of Magnetic Resonance in Medicine, Honolulu, HI, 2009. p. 4557.
11. Gallichan D, Cocosco CA, Dewdney A, Schultz G, Welz A, Hennig J, Zaitsev M. Simultaneously driven linear and nonlinear spatial encoding fields in MRI. Magn Reson Med 2011;65:702–714.
12. Pruessmann KP, Weiger M, Bornert P, Boesiger P. Advances in sensitivity encoding with arbitrary k-space trajectories. Magn Reson Med 2001;46:638–651.
13. Gallichan D, Cocosco CA, Dewdney A, Schultz G, Welz A, Hennig J, Zaitsev M. Simultaneously driven linear and nonlinear spatial encoding fields in MRI. Magn Reson Med 2011.
14. Stockmann JP, Ciris PA, Galiana G, Tam L, Constable RT. O-space imaging: highly efficient parallel imaging using second-order nonlinear fields as encoding gradients with no phase encoding. Magn Reson Med 2010;64:447–456.
15. Welz A, Cocosco C, Dewdney A, Schmidt H, Jia F, Korvink J, Hennig J, Zaitsev M.PatLoc gradient insert coil for human imaging at 3T. In: Proceedings of the ESMRMB, Antalya, Turkey, 2009. p. 316.
16. Juchem C, Nixon TW, Diduch P, Rothman DL, Starewicz P, de Graaf RA. Dynamic shimming of the human brain at 7 Tesla. Concepts Magn Reson Part B: Magn Reson Eng 2010;37:116–128.
17. Juchem C, Nixon TW, McIntyre S, Rothman DL, de Graaf RA. Magnetic field modeling with a set of individual localized coils. J Magn Reson 2010;204:281–289.
18. Juchem C, Nixon TW, McIntyre S, Rothman DL, de Graaf RA. Magnetic field homogenization of the human prefrontal cortex with a set of localized electrical coils. Magn Reson Med 2010;63:171–180.
19. Lin FH, Witzel T, Nummenmaa A, Vesanen P, Ilmoniemi RJ, Belliveau JW. Multi-dimensional encoded (MDE) magnetic resonance imaging. Proc Int Soc Magn Reson Med 2011:480.
20. Witschey W, Cocosco C, Gallichan D, Schultz G, Weber H, Welz A, Hennig J, Zaitsev M. Localization by nonlinear phase preparation and K-space trajectory design (GradLoc). Proc Int Soc Magn Reson Med 2011:2805.
21. Schneider J, Haas M, Ohre S, Lehr H, Ruhm W, Post H, Hennig J, Ullmann P. Parallel spatially selective excitation using nonlinear non-bijective PatLoc encoding fields: experimental realization and first results. Proc Int Soc Magn Reson Med 2011:211.
22. Weber H, Gallichan D, Schultz G, Witschey W, Welz A, Cocosco C, Hennig J, Zaitsev M. ExLoc: excitation and encoding of curved slices. Proc Int Soc Magn Reson Med 2011:2806.